https://doi.org/10.1016/j.electacta.2019.03.031

Self-Reconstruction Mechanism in $NiSe_2$ Nanoparticles/Carbon Fiber Paper Bifunctional Electrocatalysts For Water Splitting

*Lingling Zhai, Chun Hin Mak, Jiasheng Qian, Shenghuang Lin, Shu Ping Lau**

Keywords: nickel diselenide, bifunctional electrocatalyst, hydrogen evolution reaction, oxygen evolution reaction, water splitting

L. Zhai, C. H. Mak, Dr. J. Qian, Dr. S. Lin, Prof. S. P. Lau.
Department of Applied Physics
The Hong Kong Polytechnic University
Hung Hom
Hong Kong S.A.R., China
*Corrsponding author. E-mail: apsplau@polyu.edu.hk

Abstract

Developing efficient bifunctional electrocatalysts and gaining fundamental understanding of reaction mechanisms are crucial for practical water splitting. Herein, a bifunctional $NiSe_2$ nanoparticles/carbon fiber paper (NSN/CFP) electrode is fabricated by the pyrolysis of $Ni(NO_3)_2$ on CFP, followed by a selenization step. The as-prepared electrocatalysts exhibit superior overall water splitting behavior in 1 M KOH with low overpotentials of 145 mV and 280 mV at current densities of 10 $mA \cdot cm^{-2}$ for hydrogen evolution reaction (HER) and oxygen evolution reaction (OER), comparable to the performance of 20% Pt/C and RuO_2. Detailed compositional and morphological studies reveal that the $NiSe_2$ gradually transforms into an amorphous $Ni(OH)_2$/NiOOH heterojunction during both HER and OER in alkaline medium. Based on these experimental results, an oxidation-induced self-reconstruction mechanism is proposed. Owing to the highly-oxidized $Ni(OH)_2$/NiOOH active species, the self-reconstructed structure enhances the water splitting under fixed potentials for a prolonged time of 96 h with negligible current degradation. This work not only provides a facile route to fabricate efficient and stable electrocatalysts for large-scale water splitting but also reveals an underlying structural evolution mechanism, which guides the rational design of heterogeneous catalysts.

1. Introduction

Hydrogen energy is regarded as one of the most promising clean substitutions in fuel consumption. From this expectation, scalable production of hydrogen from water splitting has been extensively studied[1-3]. Over the past few years, varieties of non-noble transition metal catalysts have been investigated toward efficient HER and OER, such as metal dichalcogenides, phosphides and carbides ($MoS_{2[4-7]}$, WSe_2[8, 9], $CoS_{2x}Se_{2(1-x)[10]}$, Ni_2P[11] and Mo_2C[12, 13]) for HER and first-row transition metal (Fe, Co and Ni) hydroxides[14-16]/oxides[17, 18] for OER. However, it is still challenging to trigger both HER and OER with high activity in a balanced electrolyte due to their opposite pH range requirement. Additionally, alkaline water electrolysis method has been prevalent for several decades and is regarded as a mature technology in industry owing to its low corrosion rate and cost. Therefore, it is highly desirable to develop bifunctional catalysts for both HER and OER in alkaline medium for efficient industrial application.

Among the various electrocatalysts that have been studied, $NiSe_2$ is one of the few Ni-based catalysts that can be applied for both HER and OER. By decorating with other metals[19, 20] or metal oxides[21], $NiSe_2$-based catalysts have shown superior performance in water splitting. For instance, $NiSe_2$ ultrathin nanowires[21] was synthesized by a solvothermal method. The abundant 1D nanowires not only promoted interfacial electron transfer but also exposed more active sites by doping with NiO_x. However, it is still critical and challenging to increase the active sites and improve its intrinsic conductivity through a simple way. From this perspective, a low-dimensional nanostructured $NiSe_2$ grown on a conductive substrate could be a good strategy to solve this problem. Thus, in this work, we chose $NiSe_2$ nanoparticles and conductive carbon fiber paper to a form a 3D porous structure in order to maximize the exposed active edges. Though considerable efforts have been made to investigate Ni-based catalysts for prolific HER and OER, most previous

works were focused on either rational designing of the nanostructures, optimizing elemental compositions or seeking more facile routes to synthesize these catalysts. The stability of the catalyst, the possible phase transformation and the “real” active sites for both HER and OER are rarely discussed. Therefore, it is also significant to further investigate the compositional, structural and morphological changes after reaction to better understand the “true” nature of the catalysts.

Herein, we report a facile approach to fabricate homogeneous nickel diselenide ($NiSe_2$) nanoparticles anchored on carbon fiber paper (CFP) as bifunctional electrocatalysts for efficient HER and OER. The nanoparticles were prepared using nickel oxide (NiO) nanoparticles followed by a selenization process. CFP acts not only as a substrate, but also effectively reduces the aggregation of nanoparticles, so as to form a homogeneous interface. Owing to its intrinsic conductivity, CFP also helps to promote the catalytic rate by efficient charge exchange. The as-prepared NSN/CFP can directly act as both cathode and anode to drive overall water splitting, which can achieve a high current density of 100 $mA \cdot cm^{-2}$ with overpotentials of 232 mV for HER and 370 mV for OER in 1M KOH. The excellent performance is comparable to the state-of-the-art non-precious metal-based bifunctional catalysts[22, 23]. Moreover, various techniques were employed to probe the phase changes prior to and post catalysis, demonstrating that the surface $NiSe_2$ are gradually fully oxidized into an amorphous $Ni(OH)_2$/NiOOH layer with high-valence state for both HER and OER.

2. Results and discussion

2.1. Material Characterizations

The as-prepared NSN/CFP was first examined by X-ray diffraction (XRD) to analyze the crystallographic structure and phase purity. For comparison, $NiSe_2$ clusters (NSC) were also

prepared by a hydrothermal method[24], it was drop-casting onto the bare CFP with the same mass loading as NSN/CFP, denoted as NSC/CFP. For the preparation of NSN/CFP, nickel oxide (NiO) was first prepared by the pyrolysis of nickel nitrate. X-ray diffraction (XRD) pattern of the as-prepared NiO is presented in **Fig. S1**, which matches well with the cubic NiO phase (JCPDS 65-2901). After selenization, the NiO transformed into $NiSe_2$ completely. As shown in **Fig. 1**a, the $NiSe_2$ nanoparticles display characteristic peaks at 29.9°, 33.6°, 36.9° and 50.8° corresponding to the (200), (210), (211) and (311) planes, respectively, which is consistent with cubic structured $NiSe_2$ (JCPDS 65-1843). No other impurities such as selenium or NiO are observed, indicating the reaction was controlled precisely. The full width at half maximum (FWHM) value of the (210) plane of NSN (0.132) is much less than that of NSC (0.307), indicating a higher crystallization and reduced particle size. This is also consistent with the TEM results to be discussed in the next section.

The surface chemical states of the NSN/CFP were further investigated via X-ray photoelectron spectroscopy (XPS). As shown in **Fig. S2**, the survey spectrum indicates obvious peak signals of Se, C, O and Ni elements, and the signal of O element is due to the surface oxidation[23] which has been widely reported. **Fig. 1**b and **1**c presents the high-resolution XPS spectra of Ni 2p and Se 3d peaks, respectively. The two main peaks of Ni 2p3/2 and Ni 2p1/2 can be resolved into three bands respectively, of which the N1 and N4 peaks locate at 853.6 eV and 871.1 eV come from Ni^{2+} ions. And the N2 and N5 peaks at 855.2 eV and 873 eV, are caused by the surface oxide Ni-O bond[25, 26]. The residual N3 and N6 peaks at 859.8 eV and 877.5 eV, can be assigned to satellite peaks with higher binding energy. For Se, the 3d peak can be resolved into three bands, of which the peaks at 54.9 eV and 55.7 eV represent the splitting of Se $3d_{5/2}$ and Se $3d_{3/2}$ branches.

And the peak at 59 eV implies the surface oxidation of Se species. These results reveal the surface condition of the NSN/CFP and are consistent with other literatures[27, 28].

Scanning electron microscopy (SEM) and transmission electron microscopy (TEM) were further conducted to examine the morphology and structure details of NSN/CFP. As shown in **Fig. S3**, the CFP is composed of hundreds of interlaced carbon fibers. This irregular stacking forms a 3D porous structure which largely facilitates the loading of $NiSe_2$. After selenization, the surface is homogeneously covered by a layer of $NiSe_2$ nanoparticles. Elemental mapping (**Fig.1**d) reveals the uniform distribution of Ni and Se, and the atomic ratio is close to 1:2 (**Fig. S4**). As shown in **Fig. 1**e and **S5**a, the $NiSe_2$ nanoparticles (red circles) are well dispersed with clear edges. Owing to the high hydrophilcity of the porous carbon fiber, the nanoparticles can firmly root in the carbon layer (inset of **Fig. 1**e) with size distribution ranging from 100 to 200 nm, making this NSN/CFP a binder-free electrode. The nano-scale size as well as the densely coverage of the nanoparticles provide multiple catalytic sites. In contrast, the hydrothermal-synthesized NSCs are aggregated seriously in micrometer scale as shown in **Fig. S5**b. Selected area electron diffraction (SAED) pattern (**Fig. 1e,** inset) indicates the highly crystalline nature of the $NiSe_2$ nanoparticles with typical crystal faces of (200), (311), (411) and (321), while the SAED pattern of the NSCs (**Fig. S5**c) is more scattered and attributed to the thick aggregation of the clusters. High-resolution TEM (HRTEM) images and associated reduced fast Fourier transform (FFT) of the $NiSe_2$ nanoparticles and clusters are shown in **Fig. 1**f and **S5**d, respectively. The inter fringe distance of 2.98 Å and 2.67 Å correspond to the (200) and (210) planes of the cubic $NiSe_2$ phase are observed. The reduced FFT patterns obtained from red square areas indicating the crystalline nature of both NSNs and NSCs.

2.2. Electrocatalytic Performance toward HER

The electrocatalytic activities of the NSN/CFP for HER were conducted in Ar-saturated 1M KOH at a scan rate of 5 mV/s. The 20% Pt/C, bare carbon fiber paper and NSC/CFP were also tested as contrastive samples. All of the potentials are referred to reversible hydrogen electrode (RHE) and have been iR corrected unless noted. Before testing, the reference electrode was calibrated with respect to RHE (**Fig. S6).** As shown in **Fig. 2**a, the 20% Pt/C displays the lowest overpotential (92 mV) at a current density of 10 $mA{\cdot}cm^{-2}$, while the NSN/CFP reveals superior catalytic activity when the overpotential exceeds 220 mV. The NSN/CFP electrode only needs overpotentials of 145, 170 and 232 mV to obtain cathodic current densities of 10, 20 and 100 $mA \cdot cm^{-2}$, outperforming many transition metal sulfides[29, 30] or phosphides[31, 32] reported recently. This high kinetic is also confirmed by the low Tafel slope as present in **Fig. 2**b. In comparison, the NSC/CFP electrode shows much inferior performance with a small current density change in a wide potential range. Furthermore, the electrochemical active surface area (ECSA) was estimated based on double-layer capacitance (C_{dl}, **Fig. 2**c) using cyclic voltammetry (CV) measurements in the range of no obvious Faradaic process (**Fig. S7**). Notably, the ECSA value of NSN/CFP ($1202.5cm^2$) is almost ten-fold than that of NSC/CFP (132.5 cm^2). Since the ECSA reflects the surface roughness condition and ratio of active sites, this prominent increase may be due to several reasons: (i) the nanostructured $NiSe_2$ particles have a much larger specific surface area to offer more reaction domains; (ii) the porous carbon fiber can absorb more dissociate water molecules thus provide sufficient reactant; (iii) the tight bonding between the metallic $NiSe_2$ nanoparticles and the conductive carbon fiber paper formed strong electrochemical coupling.

In order to verify the hypothesis of the enhanced charge-transfer property, electrochemical impedance spectroscopy (EIS) measurements were conducted at a current density of 10 $mA{\cdot}cm^{-2}$.

As shown in the corresponding Niquist plot **(Fig. 2**d**)**, the two semicircles in impedance curve of the 20% Pt/C indicate that there are two charge transfer resistances obstructing the electron transport, this discontinuous pathway increases the energy barriers for hydrogen desorption. In contrast, both the NSN/CFP and NSC/CFP have only one semicircle, demonstrating the efficient charge transfer on the interface between $NiSe_2$ and carbon fiber paper. Based on the Bode Plots, equivalent circuits were then simulated. As shown in **Fig. S8** and **Table. S1**, the electrolyte resistance (R_s) of the NSN/CFP (2.0 Ω) and NSC/CFP (2.1 Ω) are much lower than that of 20% Pt/C (11.6 Ω), indicating the preferable adhesion between the water molecule and the electrode. Particularly, the charge-transfer resistance (R_{ct}) of the NSN/CFP (4 Ω) is only 34% to that of NSC/CFP (11.8 Ω). This is due to the strong connection between the $NiSe_2$ nanoparticles and carbon fiber paper as discussed before.

2.3. Electrocatalytic Performance toward OER

As a four-electron oxidation process, OER ($4OH^- \rightarrow O_2+2H_2O+4e^-$) requires more thermodynamic and kinetic energy which is much harsher than HER. Therefore, OER is considered as the major obstacle of the overall water splitting rate with a considerable requirement of 1.23 V ideally. Despite $NiSe_2$-based electrocatalysts have been intensively reported to drive HER, their OER performance are rarely studied. In order to avoid the influence of double-layer capacity on current density, the linear sweep voltammetry (LSV) curve was recorded at a slow scan rate of 0.1 $mV \cdot s^{-1}$. As shown in **Fig. 3**a, the NSN/CFP requires an overpotential of only 280 mV to achieve an anodic current density of 10 $mA \cdot cm^{-2}$, which is much lower than the NSC/CFP (370 mV), and even RuO_2 catalyst (330 mV). The small peak of LSV curve at 1.37 V can be assigned to the oxidation of Ni^{2+} to Ni^{3+}, this oxidation effect is consistent with other literatures[23, 33]. The

remarkable performance of the NSN/CFP upon OER is further confirmed with an anodic current density of 100 $mA \cdot cm^{-2}$ at a small overpotential of 370 mV. The Tafel slope (**Fig. 3**b) of the NSN/CFP (81 $mV \cdot dec^{-1}$) is lower than the NSC/CFP (92 $mV \cdot dec^{-1}$), indicating a higher reaction kinetics. Indeed, during the OER process, O_2 bubbles start to be visible at 1.46 V and became drastic as the current density over 20 $mA \cdot cm^{-2}$. ~~As shown in **Figure S9**, cyclic voltammetry is conducted in the range of 1.025 - 1.125 V to calculate the ECSA. The comparison of C_{dl} (**Figure 3c**) reveals that the ECSA value of NSN/CFP is more than tenfold higher than that of NSC/CFP.~~ This preferable catalytic activity of NSN/CFP is also confirmed by EIS measurement as shown in **Fig. 3**c. The R_{ct} value of the NSN/CFP (2.2 Ω) is much smaller than the NSC/CFP (8.4 Ω), demonstrating the fast electron transport. In general, the excellent performance of the NSN/CFP toward OER is outperforming many non-precious metal catalysts, including Cu_2O[34] and CoO_x[35].

2.4. Mechanism Discussion

Compared with the well-documented acidic HER mechanism, the fundamental theories of alkaline HER ($2H_2O+2e^- \rightarrow H_2+2H^+$) and OER ($4OH^- \rightarrow O_2+2H_2O+4e^-$) remain inconclusive. Recent research reveals the generation of NiOOH or $Ni(OH)_2$ phases on nickel-based chalcogenides or phosphides during the OER process[36]. The composition of the post catalysis products is controversial which can be classified into oxides, hydroxides and oxyhydroxides[36-39]. The reversible faradaic reaction can be described as: $Ni(OH)_2 + OH^- \rightleftharpoons NiOOH + H_2O + e^-$[40]. Since the anions in group VIA-VIIIA (C, N, P, S, Se, Te) have strong similarities in chemical properties, it is highly possible that similar oxidation effect happens in our $NiSe_2$-based system. Thus, further investigations are needed to systematically investigate the phase evolution.

In order to eliminate the interference of the changing potential and also precisely control the reaction degree, chronopotentiometric method was used to prepare the contrastive samples after both HER and OER. The fresh NSN/CFPs were applied at constant potentials for 0.5 h, the current densities are around 10 $mA \cdot cm^{-2}$. SEM images (**Fig. S9**) show no obvious morphological change after reactions, while the corresponding EDX analysis (**Fig. 4**a) imply an oxidation process during both HER and OER. After HER, the composition of Ni almost no changed, while the ratio of Se to Ni decreased from 2.0 to 0.43, indicating Se leaching from the carbon fiber. Additionally, the appearance of O implies the oxidation of $NiSe_2$. Notably, the composition after OER reveals a much lower ratio of Se and a dramatically increase in O, demonstrating a much deeper oxidized level. This difference in phase evolution rate is also confirmed by XRD spectra as shown in **Fig. 4**b, the characteristic peaks of the $NiSe_2$ are weakened after HER but almost totally disappeared after OER, indicating the $NiSe_2$ was decomposed more severely during OER.

The specific compositional changes were further analyzed by Raman scattering characterization and XPS. As shown in **Fig. S10**, the peaks at 154.9, 170.2, 215.8 and 246.8 cm^{-1} are corresponding to the Tg, Eg, Ag and Tg modes of $NiSe_2$, respectively. These observations are in good agreement with previous reports on pyrite $NiSe_2$[41, 42]. After HER and OER aging, the intensity of the characteristic peaks decreased, demonstrating the reduced ratio of the $NiSe_2$ after reaction. The two new broad peaks located at 340 and 557 cm^{-1} can be attributed to the Eg mode of Ni-OH[43, 44] and vibration of Ni-O stretching mode[45, 46], respectively. It should be noticed that the Eg band is blueshifted by around 25 cm^{-1}, which is attributed to the reversible transition between $Ni(OH)_2$ and NiOOH. The samples were then detected by XPS measurement to investigate the compositional changes. As shown in **Fig. S11**, the O 1s peak intensity is increased after HER and OER, which could be associated with the oxidation of Ni. From the spectra comparison of Ni 2p

region (**Fig. 4**c**, Table S2**), it can be seen that these deconvoluted peaks shifted by 2.3 eV after HER and OER. The Ni-Se peak disappeared after HER and OER, meaning the metastable surficial Se_2^{2-} fell off and dissolved in solution under the applied potential. Two new peaks raised at 855.9 eV (N1') and 857 eV (N2') which is due to the oxidized reaction on the catalyst surface. It is noted that the phase transition sequence in nickel based alkaline batteries is: $Ni^0 \rightarrow NiO_x \rightarrow Ni(OH)_2 \rightarrow$ NiOOH[45]. Unsurprisingly, the binding energy order of these compounds is also the same: Ni < NiOx < $Ni(OH)_2$ < NiOOH[47]. Then considering that the binding energy of N1' and N2' are larger than N2 (855.2 eV), the N1' and N2' peaks can be ascribed to $Ni(OH)_2$ and NiOOH, respectively. After HER and OER aging, the peak intensities of Se 3d (**Fig. 4**d) for Se_2^{2-} at 54.9 eV and 55.7 eV decreased dramatically while that of the oxidation state Se increased largely, indicating the dominant ratio of selenide oxide. This phase evolution was also confirmed by TEM characterization as shown in **Fig. 5**. After HER, the whole nanoparticle becomes amorphous with some lattice distortion. The SAED pattern also displays a typical (103) face of $Ni(OH)_2$ (JCPDS 22-0444). In order to investigate the final conditions of the NSN/CFP, the samples were further conducted at current densities of 10 $mA \cdot cm^{-2}$ for 24 h. The XRD characterization reveals that the peaks of $NiSe_2$ are disappeared as shown in **Fig. S12**, meaning that all the $NiSe_2$ nanocrystals were converted to amorphous nickel hyoxide/oxyhydroxide. Based on the various characterizations above, we conclude that crystalline $NiSe_2$ will totally evolve into amorphous $Ni(OH)_2$/NiOOH during both HER and OER in alkaline medium. The difference is the phase transition during OER is much faster and severely.

Given the aforementioned results, we propose a possible self-reconstruction mechanism as shown in **Fig. 6**a:

$$Ni^{2+} + Se_2^{2-} + 2OH^- + xO_2 \rightarrow Ni(OH)_2 + 2SeO_x + 2e^- \quad (1)$$

$$Ni(OH)_2 + OH^- \rightleftarrows NiOOH + H_2O + e^- \quad (2)$$

In the initial of the reaction, $NiSe_2$ nanoparticles are unstable when a potential applied, the outermost layer of the $NiSe_2$ will ionize in strong KOH solution. Then Ni^{2+} joins OH^- while Se_2^{2-} leaches out and combines with the dissolved oxygen. This step transforms the pyrite-type $NiSe_2$ into lamellar-type $Ni(OH)_2$, the dissociated oxygen acts as oxidizing agent and generates SeO_x. With a higher degree of polarization (charging), the formed metastable nickel hydroxide evolves into oxyhydroxide phase with a lattice expanison[47]. In this process, the surface Se_2^{2-} acts like a sacrificial template, the residual Ni^{2+} totally reconstructs into amorphous $Ni(OH)_2$/NiOOH heterojunctions with high-valence states. In order to evaluate the influence of the oxidation effect on the catalytic performance, LSVs at different aging stages and the corresponding C_{dl} values were measured. As shown in **Fig. S13** and **S14**, during the transformation process the catalytic performance are improved for both HER and OER and the active surface areas are also greatly enlarged. While a degradation of the OER performance is also observed due to the detachment of the active species (**Fig. S15**) caused by the harsh oxidation effect. Thus, the synergistic effect among the $Ni(OH)_2$/NiOOH and the irregular morphology promote more exposed active sites, leading to an enhanced catalytic activity.

2.5 Long-term Durability and Overall Water Splitting

The durability of the NSN/CFP electrode for both HER and OER in alkaline was examined by applying steady potentials (-0.17 V for HER and 1.53 V for OER) for 96 h. **Fig. 6**b shows the chronoamperometry curves of the NSN/CFP electrodes for both HER and OER. Clearly, the NSN/CFPs can maintain stable and continuous catalytic activities. During the OER process, the current density reduced gradually from 14.1 to 10.2 $mA \cdot cm^{-2}$ in the first 24 h and kept almost no

changed in the next 72 h. The current density of HER decreased from 11.2 $mA \cdot cm^{-2}$ to 9.9 $mA \cdot cm^{-2}$ by a ratio of 11.6%, this slow decline indicates its huge potential for practical application. Interestingly, a "self-recovery" process can be observed during both HER and OER process. For HER, the current density is maintained at -11 $mA \cdot cm^{-2}$ in the first 12 h. From 13 to 24 h, the current density increases gradually and reaches a maximum at -13 $mA \cdot cm^{-2}$, then the current density decreases to its original value. Similar variation trend is also found during OER, the cycle repeats roughly in a 24 h period. The experiments were repeated several times with various applied potentials and similar trends can be observed. Fan *et al.* and others[48-50] reported the similar recovery process in their systems and attributed their observations to the adequate activation of catalyst, or trapping and releasing of gas bubbles on the surface. In our case, we ascribe this phenomenon to the unbalanced rate between H^+/OH^- adsorption and H_2/O_2 desorption. As we discussed before, the $NiSe_2$ has fully evolved into $Ni(OH)_2$/NiOOH during both long-time HER and OER run, since transition metal hydroxides have strong abilities to dissociate water[51], then we speculate that the electrode surface was covered by a high ratio of H^+/OH^-, resulting in the accumulation of current and hysteresis of gas desorption.

Based on the electrochemical characterization of HER and OER, an alkaline electrolytic cell was fabricated by using the NSN/CFPs as bifunctional electrodes for both cathode and anode in 1 M KOH medium. Notably, appreciable hydrogen bubbles can be observed at 1.55 V, the current density can reach 10 $mA \cdot cm^{-2}$ at a potential of 1.66 V (**Fig. S16**). The comparison of HER and OER performance for the NSN/CFP with other non-noble catalysts are summarized in **Table 1**. It is prominent that the NSN/CFP electrode is rivaling most other non-precious metal bifunctional catalysts for overall alkaline water splitting. Furthermore, we fabricated a solar power-driven water splitting device to assess the electrode in real solar energy application. By powering a 2 V solar

panel, the evolved hydrogen and oxygen bubbles were observed clearly (**Fig. 6b**, inset and **Movie S1**, Supporting Information), demonstrating that the NSN/CFP is a promising electrode for practical water electrolysis application.

3. Conclusion

In summary, we fabricate a bifunctional binder-free NSN/CFP electrode for water splitting by homogeneously anchoring the metallic $NiSe_2$ nanoparticles on the conductive cylindrical carbon fibers. The NSN/CFP exhibits low overpotentials (145 mV for HER, 280 mV for OER) at current densities of 10 $mA \cdot cm^{-2}$ with superior durability (96 h), revealing its ability as a bifunctional electrocatalyst. Based on systematical characterizations of the $NiSe_2$ prior to and post electrocatalysis, the co-existence of highly-oxidized $Ni(OH)_2$/NiOOH were demonstrated, a self-reconstruction mechanism was deduced as well. The remarkable bifunctional performance can be ascribed to the reconstructed surface that provide multiple exposed active sites as well as the conductive carbon fiber paper that offers a 3D porous charge transfer pathway. This work not only provides a facile and low-cost strategy to prepare highly active electrocatalysts, but also offers insights into the identification of phase evolution during electrolysis reactions.

4. Experimental section

4.1 Chemicals and reagents

All chemicals were purchased from Sigma-Aldrich and used as received. The carbon fiber paper (HCP030) was bought from Hesen Group.

4.2 Preparation of $NiSe_2$ nanoparticles/carbon fiber paper electrode (NSN/CFP)

NSN/CFP was synthesized referred to previous method[52] with some modified. In brief, a precursor solution was prepared by dissolving 30wt% nickel (II) nitrate hexahydrate and 5wt% polyvinylpyrrolidone (PVP) in dimethylformamide (DMF) under vigorous stir in a 10 ml vial at 65 °C for 2 h. A 3 cm × 1 cm bare carbon fiber paper was cleaned by oxygen plasma and then immersed into the solution for one night. After taken out and dried naturally, the carbon fiber paper was placed at the center of a tube furnace and pyrolyzed at 600 °C for 2 h under Ar atmosphere. After cooled down naturally, selenium powder was placed at the upstream side of the furnace. The tube was first flushed with Ar gas, and then elevated to 450 °C with an increasing rate of 30 °C·min^{-1}, while the selenium precursor was kept at ~300 °C. The reaction was kept for 25 min with a flow rate of 100 sccm. After cooled down naturally, the in-situ grown NSN/CFP electrode was fabricated. The mass loading is around 1.8 - 2.0 mg/cm^2 by calculating the increase in weight after reaction.

Carbon fiber paper was chosen as the substrate not only because its high electrical conductivity but also the excellent resistance to corrosion in both acidic and alkaline solutions. Polyvinylpyrrolidone (PVP, Mw ≈ 30000) was selected as thickening, complexation and structure-directing agent.

4.3 Preparation of $NiSe_2$ cluster/carbon fiber paper electrode (NSC/CFP)

$NiSe_2$ clusters were prepared by a hydrothermal method referred to previous method[24] with some modified. Typically, 0.1 mol NaOH, 1 mmol $NiCl_2 \cdot 6H_2O$, 2 mmol Se powder and 1.6 mmol Ethylene Diamine Tetraacetic Acid (EDTA) were dissolved in 30 mL deionized water. After stir for 30min, the aqueous solution was transferred into a 50 mL Teflon lined autoclave. Then, the sealed autoclave was put in an oven and maintained at 180 ºC for 12 h. After cooled down naturally, the precipitate was centrifuged and washed with deionized water and ethanol for several times,

then dried at 50 ºC for 12 h. Finally, the powder was mixed in deionized water/ethanol solution with 0.1 wt% Nafion and sonicated for 30 min to generate a homogeneous ink, and drop-casted on the bare carbon fiber paper with the same mass loading as the $NiSe_2$ nanoparticles.

4.4 Material characterization

The phase identifications of the as-synthesized samples were characterized by powder X-ray diffraction (XRD) on a Rigaku Smartlab X-ray diffractometer using Cu Kα radiation (λ = 1.5418 Å) at 45 kV and 200 mA. The XRD patterns were indexed and quantitatively analyzed according to the ICDD PDF-4 database. The morphology, microstructure and energy-disperse X-ray spectra (EDX) were investigated by scanning electron microscope (SEM) using a Tescan VEGA3 microscope equipped with X-max5 EDX (Oxford Instruments). Transmission electron microscopy (TEM), high resolution transmission electron microscopy (HRTEM) and selected area electron diffraction (SAED) were carried out on a JEOL JEM-2100F at 200kV, using the holey carbon-coated copper grid. X-ray photoelectron spectroscopy (XPS) measurements were conducted using an ThermoFisher EscaLab 250Xi at 1° angle of emission. The source was a monochromatic Al Kα (Ephoton = 1486.6 eV) with a 10 mA filament current and a 12 keV filament voltage. Measurements were carried out in field of view 2 with a 110 mm aperture and a pass energy of 40 eV. In order to compensate for the charging of the sample, a consistent charge neutralization was verified by observing adventitious C 1s peak at ≈ 284.8 eV for all samples.

4.5 Electrochemical measurements

All electrochemical measurements were performed at room temperature using a standard three-electrode system on an electrochemical workstation (Solartron 1470E) with graphite carbon rod as counter electrode and Hg/HgO (1M KOH solution) as reference electrode. Polyimide tape was employed to define the 1 cm^2 area on the as-fabricated NSN/CFP and NSC/CFP working

electrodes. The performance of commercial 20% Pt/C catalyst and RuO_2 were tested on the glassy carbon (diameter = 3 mm) as working electrodes with a mass loading of 0.283 $mg \cdot cm^{-2}$. The Hg/HgO electrode was calibrated in H_2 saturated electrolyte with respected to reversible hydrogen electrode (RHE) using Pt wire as working electrode and graphite rod as counter electrode. The calibration was performed using cyclic voltammetry (CV) at a scan rate of 1 $mV \cdot s^{-1}$, and the average of the two potentials at which the current crossed zero was taken as the thermodynamic potential for the hydrogen electrode reaction (Figure S6). Linear sweep voltammetry (LSV) was conducted at a scan rate of 5 $mV \cdot s^{-1}$ and 0.1 $mV \cdot s^{-1}$ for HER and OER, respectively. CV measurements were carried out at different scan rates of 2, 4, 6, 8, 10 and 12 $mV \cdot s^{-1}$ to estimate the double-layer capacitance (C_{dl}). The electrochemical impedance spectroscopy (EIS) measurements were carried out in the frequency range from 10^6 to 0.01 Hz with an AC amplitude of 10 mV. The applied potentials were set at current densities of 10 $mA \cdot cm^{-2}$.

Declarations of interest

The authors declare no competing financial interest.

Acknowledgements

This work was financially supported by the PolyU grant (1-ZVGH) and the Research Grants Council of Hong Kong (Project no. PolyU 153030/15P).

Appendix A. Supplementary data

Supplementary data to this article can be found online at

References

[1] Z.W. Seh, J. Kibsgaard, C.F. Dickens, I. Chorkendorff, J.K. Nørskov, T.F. Jaramillo, Combining theory and experiment in electrocatalysis: Insights into materials design, Science, 355 (2017) eaad4998.

[2] S. Lin, Y. Liu, Z. Hu, G. Bai, Y. Li, H. Yuan, Y. Xue, L. Rogée, J. Hao, X. Zhang, Enhancement of photo-electrochemical reactions in $MAPbI_3$/Au, Mater. Today Energy, 9 (2018) 303-310.
[3] S. Lin, Y. Liu, Z. Hu, W. Lu, C.H. Mak, L. Zeng, J. Zhao, Y. Li, F. Yan, Y.H. Tsang, Tunable active edge sites in $PtSe_2$ films towards hydrogen evolution reaction, Nano Energy, 42 (2017) 26-33.
[4] Y.C. Chen, A.Y. Lu, P. Lu, X. Yang, C.M. Jiang, M. Mariano, B. Kaehr, O. Lin, A. Taylor, I.D. Sharp, Structurally Deformed MoS_2 for Electrochemically Stable, Thermally Resistant, and Highly Efficient Hydrogen Evolution Reaction, Adv. Mater., 29 (2017).
[5] S. Xu, D. Li, P. Wu, One‐pot, facile, and versatile synthesis of monolayer MoS_2/WS_2 quantum dots as bioimaging probes and efficient electrocatalysts for hydrogen evolution reaction, Adv. Funct. Mater., 25 (2015) 1127-1136.
[6] Y. Yang, H. Fei, G. Ruan, C. Xiang, J.M. Tour, Edge‐oriented MoS_2 nanoporous films as flexible electrodes for hydrogen evolution reactions and supercapacitor devices, Adv. Mater., 26 (2014) 8163-8168.
[7] G. Ye, Y. Gong, J. Lin, B. Li, Y. He, S.T. Pantelides, W. Zhou, R. Vajtai, P.M. Ajayan, Defects engineered monolayer MoS_2 for improved hydrogen evolution reaction, Nano Lett., 16 (2016) 1097-1103.
[8] K. Xu, F. Wang, Z. Wang, X. Zhan, Q. Wang, Z. Cheng, M. Safdar, J. He, Component-Controllable $WS_{2(1-x)}Se_{2x}$ Nanotubes for Efficient Hydrogen Evolution Reaction, Acs Nano, 8 (2014) 8468-8476.
[9] M. Zou, J. Chen, L. Xiao, H. Zhu, T. Yang, M. Zhang, M. Du, WSe_2 and $W(Se_xS_{1-x})_2$ nanoflakes grown on carbon nanofibers for the electrocatalytic hydrogen evolution reaction, J. Mater. Chem. A, 3 (2015) 18090-18097.
[10] K. Liu, F. Wang, K. Xu, T.A. Shifa, Z. Cheng, X. Zhan, J. He, $CoS_{2x}Se_{2(1-x)}$ nanowire array: an efficient ternary electrocatalyst for the hydrogen evolution reaction, Nanoscale, 8 (2016) 4699-4704.
[11] E.J. Popczun, C.G. Read, C.W. Roske, N.S. Lewis, R.E. Schaak, Highly active electrocatalysis of the hydrogen evolution reaction by cobalt phosphide nanoparticles, Angew. Chem., 126 (2014) 5531-5534.
[12] J.-S. Li, Y. Wang, C.-H. Liu, S.-L. Li, Y.-G. Wang, L.-Z. Dong, Z.-H. Dai, Y.-F. Li, Y.-Q. Lan, Coupled molybdenum carbide and reduced graphene oxide electrocatalysts for efficient hydrogen evolution, Nat. Commun., 7 (2016) 11204.
[13] S.T. Hunt, T. Nimmanwudipong, Y. Román‐Leshkov, Engineering Non‐sintered, Metal‐Terminated Tungsten Carbide Nanoparticles for Catalysis, Angew. Chem. Int. Ed., 53 (2014) 5131-5136.
[14] M.S. Burke, M.G. Kast, L. Trotochaud, A.M. Smith, S.W. Boettcher, Cobalt–iron (oxy) hydroxide oxygen evolution electrocatalysts: the role of structure and composition on activity, stability, and mechanism, J. Am. Chem. Soc., 137 (2015) 3638-3648.
[15] F. Dionigi, P. Strasser, NiFe‐Based (Oxy) hydroxide Catalysts for Oxygen Evolution Reaction in Non‐Acidic Electrolytes, Adv. Energy Mater., 6 (2016).
[16] M. Xie, L. Yang, Y. Ji, Z. Wang, X. Ren, Z. Liu, A.M. Asiri, X. Xiong, X. Sun, An amorphous Co-carbonate-hydroxide nanowire array for efficient and durable oxygen evolution reaction in carbonate electrolytes, Nanoscale, 9 (2017) 16612-16615.
[17] L. Xu, Q. Jiang, Z. Xiao, X. Li, J. Huo, S. Wang, L. Dai, Plasma‐Engraved Co_3O_4 Nanosheets with Oxygen Vacancies and High Surface Area for the Oxygen Evolution Reaction, Angew. Chem., 128 (2016) 5363-5367.

[18] L. Zhuang, L. Ge, Y. Yang, M. Li, Y. Jia, X. Yao, Z. Zhu, Ultrathin Iron‐Cobalt Oxide Nanosheets with Abundant Oxygen Vacancies for the Oxygen Evolution Reaction, Adv. Mater., 29 (2017).
[19] T. Liu, A.M. Asiri, X. Sun, Electrodeposited Co-doped $NiSe_2$ nanoparticles film: a good electrocatalyst for efficient water splitting, Nanoscale, 8 (2016) 3911-3915.
[20] Y. Sun, K. Xu, Z. Wei, H. Li, T. Zhang, X. Li, W. Cai, J. Ma, H.J. Fan, Y. Li, Strong Electronic Interaction in Dual‐Cation‐Incorporated $NiSe_2$ Nanosheets with Lattice Distortion for Highly Efficient Overall Water Splitting, Adv. Mater., (2018) 1802121.
[21] H. Li, S. Chen, H. Lin, X. Xu, H. Yang, L. Song, X. Wang, Nickel Diselenide Ultrathin Nanowires Decorated with Amorphous Nickel Oxide Nanoparticles for Enhanced Water Splitting Electrocatalysis, Small, 13 (2017).
[22] Y. Yan, B.Y. Xia, B. Zhao, X. Wang, A review on noble-metal-free bifunctional heterogeneous catalysts for overall electrochemical water splitting, J. Mater. Chem. A, 4 (2016) 17587-17603.
[23] X. Teng, J. Wang, L. Ji, W. Tang, Z. Chen, Hierarchically Structured Ni Nanotube Array-Based Integrated Electrodes for Water Splitting, ACS Sustain. Chem. Eng, 6 (2017) 2069-2077.
[24] J. Liang, Y. Yang, J. Zhang, J. Wu, P. Dong, J. Yuan, G. Zhang, J. Lou, Metal diselenide nanoparticles as highly active and stable electrocatalysts for the hydrogen evolution reaction, Nanoscale, 7 (2015) 14813-14816.
[25] Y. Ge, S.-P. Gao, P. Dong, R. Baines, P.M. Ajayan, M. Ye, J. Shen, Insight into the hydrogen evolution reaction of nickel dichalcogenide nanosheets: activities related to non-metal ligands, Nanoscale, 9 (2017) 5538-5544.
[26] D. Song, H. Wang, X. Wang, B. Yu, Y. Chen, $NiSe_2$ nanoparticles embedded in carbon nanowires as highly efficient and stable electrocatalyst for hydrogen evolution reaction, Electrochim. Acta, 254 (2017) 230-237.
[27] L. Lv, Z. Li, K.-H. Xue, Y. Ruan, X. Ao, H. Wan, X. Miao, B. Zhang, J. Jiang, C. Wang, Tailoring the electrocatalytic activity of bimetallic nickel-iron diselenide hollow nanochains for water oxidation, Nano Energy, 47 (2018) 275-284.
[28] X. Teng, J. Wang, L. Ji, Y. Lv, Z. Chen, Ni nanotube array-based electrodes by electrochemical alloying and de-alloying for efficient water splitting, Nanoscale, 10 (2018) 9276-9285.
[29] K. Zhang, W. Xiao, J. Li, J. Liu, C. Yan, Two-step preparation of porous nickel-sulfur electrode for hydrogen evolution in alkaline water electrolysis, Electrochim. Acta, 228 (2017) 422-427.
[30] D. Wang, X. Zhang, Z. Du, Z. Mo, Y. Wu, Q. Yang, Y. Zhang, Z. Wu, $CoNi_2S_4$ nanoparticles as highly efficient electrocatalysts for the hydrogen evolution reaction in alkaline media, Int. J. Hydrogen Energy, 42 (2017) 3043-3050.
[31] L. Wan, J. Zhang, Y. Chen, C. Zhong, W. Hu, Y. Deng, Varied hydrogen evolution reaction properties of nickel phosphide nanoparticles with different compositions in acidic and alkaline conditions, J. Mater. Sci, 52 (2017) 804-814.
[32] H. Tabassum, W. Guo, W. Meng, A. Mahmood, R. Zhao, Q. Wang, R. Zou, Metal‐Organic Frameworks Derived Cobalt Phosphide Architecture Encapsulated into B/N Co‐Doped Graphene Nanotubes for All pH Value Electrochemical Hydrogen Evolution, Adv. Energy Mater., 7 (2017) 1601671.

[33] H. Liang, L. Li, F. Meng, L. Dang, J. Zhuo, A. Forticaux, Z. Wang, S. Jin, Porous two-dimensional nanosheets converted from layered double hydroxides and their applications in electrocatalytic water splitting, Chem. Mater., 27 (2015) 5702-5711.
[34] H. Zhang, Z. Zhang, N. Li, W. Yan, Z. Zhu, Cu_2O@C core/shell nanoparticle as an electrocatalyst for oxygen evolution reaction, J. Catal., 352 (2017) 239-245.
[35] S. Dou, C.L. Dong, Z. Hu, Y.C. Huang, J.l. Chen, L. Tao, D. Yan, D. Chen, S. Shen, S. Chou, Atomic‐Scale CoO_x Species in Metal‐Organic Frameworks for Oxygen Evolution Reaction, Adv. Funct. Mater., 27 (2017) 1702546.
[36] X. Wang, W. Li, D. Xiong, D.Y. Petrovykh, L. Liu, Bifunctional nickel phosphide nanocatalysts supported on carbon fiber paper for highly efficient and stable overall water splitting, Adv. Funct. Mater., 26 (2016) 4067-4077.
[37] N. Jiang, B. You, M. Sheng, Y. Sun, Bifunctionality and Mechanism of Electrodeposited Nickel–Phosphorous Films for Efficient Overall Water Splitting, ChemCatChem, 8 (2016) 106-112.
[38] Z. Pu, Y. Luo, A.M. Asiri, X. Sun, Efficient electrochemical water splitting catalyzed by electrodeposited nickel diselenide nanoparticles based film, ACS Appl. Mater. Inter., 8 (2016) 4718-4723.
[39] Y. Zhang, L. Gao, E.J. Hensen, J.P. Hofmann, Evaluating the Stability of Co_2P Electrocatalysts in the Hydrogen Evolution Reaction in Both Acidic and Alkaline Electrolytes, ACS Energy Eett., (2018).
[40] Y.-Z. Su, K. Xiao, N. Li, Z.-Q. Liu, S.-Z. Qiao, Amorphous $Ni(OH)_2$@three-dimensional Ni core–shell nanostructures for high capacitance pseudocapacitors and asymmetric supercapacitors, J. Mater. Chem. A, 2 (2014) 13845-13853.
[41] H. Zhou, F. Yu, Y. Liu, J. Sun, Z. Zhu, R. He, J. Bao, W.A. Goddard, S. Chen, Z. Ren, Outstanding hydrogen evolution reaction catalyzed by porous nickel diselenide electrocatalysts, Energ. Environ. Sci., 10 (2017) 1487-1492.
[42] H. Zhou, Y. Wang, R. He, F. Yu, J. Sun, F. Wang, Y. Lan, Z. Ren, S. Chen, One-step synthesis of self-supported porous $NiSe_2$/Ni hybrid foam: an efficient 3D electrode for hydrogen evolution reaction, Nano Energy, 20 (2016) 29-36.
[43] B. Grégoire, C. Ruby, C. Carteret, Hydrolysis of mixed Ni^{2+}–Fe^{3+} and Mg^{2+}–Fe^{3+} solutions and mechanism of formation of layered double hydroxides, Dalton Trans., 42 (2013) 15687-15698.
[44] L.-F. Huang, M. Hutchison, R. Santucci Jr, J. Scully, J. Rondinelli, Improved electrochemical phase diagrams from theory and experiment: the Ni–water system and its complex compounds, J. Phys. Chem. C, 121 (2017) 9782-9789.
[45] Y.-J. Shih, Y.-H. Huang, C. Huang, Electrocatalytic ammonia oxidation over a nickel foam electrode: Role of $Ni(OH)_{2(s)}$-$NiOOH_{(s)}$ nanocatalysts, Electrochim. Acta, 263 (2018) 261-271.
[46] X. Li, L. Zhang, M. Huang, S. Wang, X. Li, H. Zhu, Cobalt and nickel selenide nanowalls anchored on graphene as bifunctional electrocatalysts for overall water splitting, J. Mater. Chem. A, 4 (2016) 14789-14795.
[47] N. Watanabe, T. Arakawa, Y. Sasaki, T. Yamashita, I. Koiwa, Influence of the memory effect on X-ray photoelectron spectroscopy and Raman scattering in positive electrode of Ni-MH batteries, J. Electrochem. Soc., 159 (2012) A1949-A1953.
[48] L. Fan, P.F. Liu, X. Yan, L. Gu, Z.Z. Yang, H.G. Yang, S. Qiu, X. Yao, Atomically isolated nickel species anchored on graphitized carbon for efficient hydrogen evolution electrocatalysis, Nat. Commun., 7 (2016) 10667.

[49] M. Fan, R. Gao, Y.-C. Zou, D. Wang, N. Bai, G.-D. Li, X. Zou, An efficient nanostructured copper (I) sulfide-based hydrogen evolution electrocatalyst at neutral pH, Electrochim. Acta, 215 (2016) 366-373.
[50] G. Jia, Y. Hu, Q. Qian, Y. Yao, S. Zhang, Z. Li, Z. Zou, Formation of hierarchical structure composed of (Co/Ni) Mn-LDH nanosheets on MWCNT backbones for efficient electrocatalytic water oxidation, ACS Appl. Mater. Inter., 8 (2016) 14527-14534.
[51] R. Subbaraman, D. Tripkovic, K.-C. Chang, D. Strmcnik, A.P. Paulikas, P. Hirunsit, M. Chan, J. Greeley, V. Stamenkovic, N.M. Markovic, Trends in activity for the water electrolyser reactions on 3d M (Ni, Co, Fe, Mn) hydr (oxy) oxide catalysts, Nat. Mater., 11 (2012) 550.
[52] D. Kong, H. Wang, Z. Lu, Y. Cui, $CoSe_2$ nanoparticles grown on carbon fiber paper: an efficient and stable electrocatalyst for hydrogen evolution reaction, J. Am. Chem. Soc., 136 (2014) 4897-4900.
[53] J. Zhou, Y. Liu, Z. Zhang, Z. Huang, X. Chen, X. Ren, L. Ren, X. Qi, J.J.E.A. Zhong, Hierarchical $NiSe_2$ sheet-like nano-architectures as an efficient and stable bifunctional electrocatalyst for overall water splitting: Phase and morphology engineering, Electrochim. Acta, 279 (2018) 195-203.
[54] H. Li, S. Chen, H. Lin, X. Xu, H. Yang, L. Song, X.J.S. Wang, Nickel diselenide ultrathin nanowires decorated with amorphous nickel oxide nanoparticles for enhanced water splitting electrocatalysis, Small, 13 (2017) 1701487.
[55] Y. Jia, L. Zhang, G. Gao, H. Chen, B. Wang, J. Zhou, M.T. Soo, M. Hong, X. Yan, G. Qian, A heterostructure coupling of exfoliated Ni–Fe hydroxide nanosheet and defective graphene as a bifunctional electrocatalyst for overall water splitting, Adv. Mater., 29 (2017) 1700017.
[56] Y. Xu, W. Tu, B. Zhang, S. Yin, Y. Huang, M. Kraft, R.J.A.M. Xu, Nickel Nanoparticles Encapsulated in Few‐Layer Nitrogen‐Doped Graphene Derived from Metal‐Organic Frameworks as Efficient Bifunctional Electrocatalysts for Overall Water Splitting, Adv. Mater., 29 (2017) 1605957.
[57] L. Yu, H. Zhou, J. Sun, F. Qin, F. Yu, J. Bao, Y. Yu, S. Chen, Z. Ren, Cu nanowires shelled with NiFe layered double hydroxide nanosheets as bifunctional electrocatalysts for overall water splitting, Energ. Environ. Sci., 10 (2017) 1820-1827.
[58] T. Tang, W.-J. Jiang, S. Niu, N. Liu, H. Luo, Y.-Y. Chen, S.-F. Jin, F. Gao, L.-J. Wan, J.-S. Hu, Electronic and morphological dual modulation of cobalt carbonate hydroxides by Mn doping toward highly efficient and stable bifunctional electrocatalysts for overall water splitting, J. Am. Chem. Soc., 139 (2017) 8320-8328.
[59] J. Song, C. Zhu, B.Z. Xu, S. Fu, M.H. Engelhard, R. Ye, D. Du, S.P. Beckman, Y. Lin, Bimetallic Cobalt‐Based Phosphide Zeolitic Imidazolate Framework: CoP_x Phase‐Dependent Electrical Conductivity and Hydrogen Atom Adsorption Energy for Efficient Overall Water Splitting, Adv. Energy Mater., 7 (2017) 1601555.
[60] K. Qu, Y. Zheng, Y. Jiao, X. Zhang, S. Dai, S.Z. Qiao, Polydopamine‐Inspired, Dual Heteroatom‐Doped Carbon Nanotubes for Highly Efficient Overall Water Splitting, Adv. Energy Mater., 7 (2017) 1602068.
[61] E. Hu, Y. Feng, J. Nai, D. Zhao, Y. Hu, X. W. D. Lou, Construction of hierarchical Ni–Co–P hollow nanobricks with oriented nanosheets for efficient overall water splitting, Energy Environ. Sci., 11 (2018) 872-880.

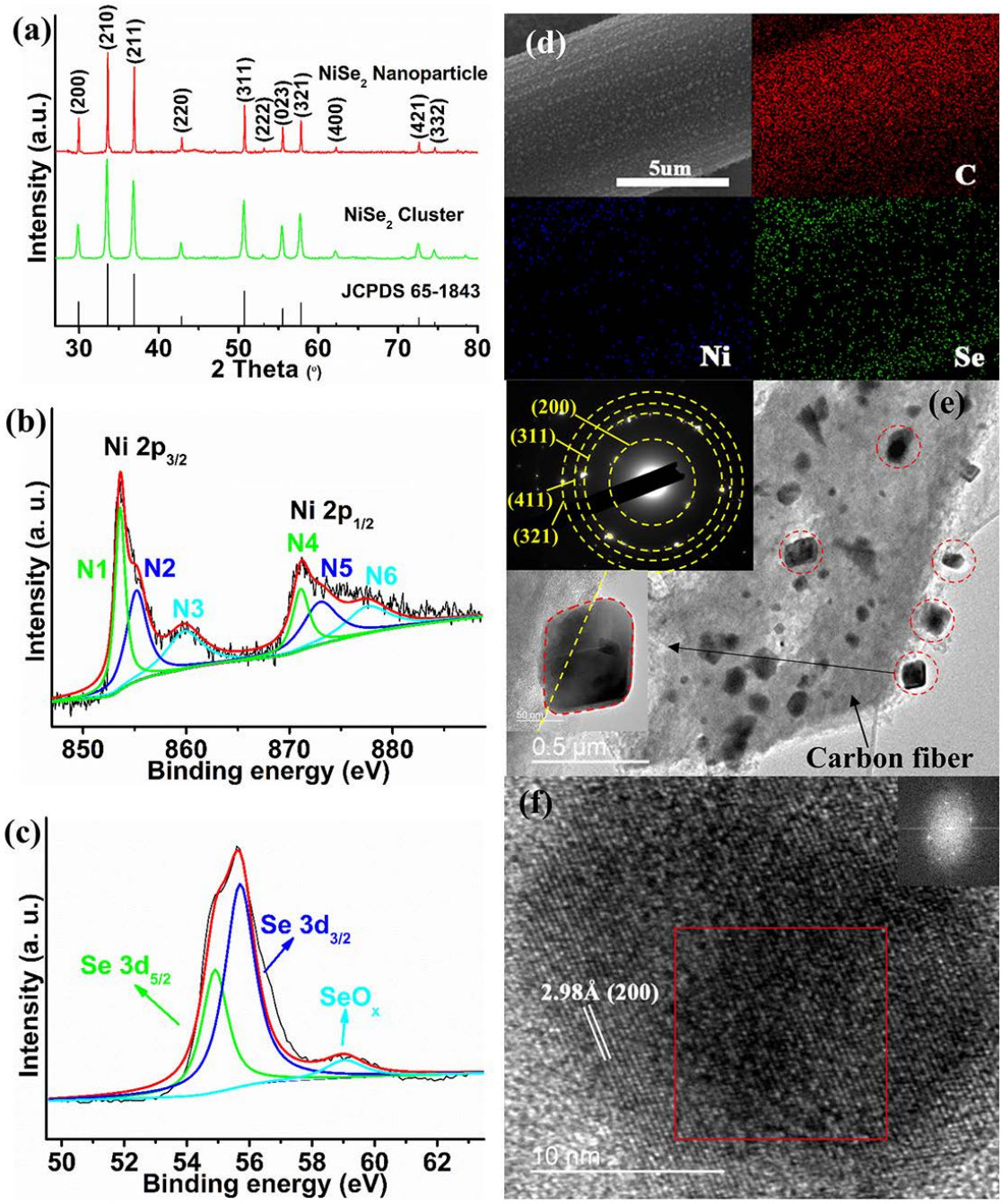

Figure 1. (a) XRD spectra of as-prepared $NiSe_2$ nanoparticles, $NiSe_2$ clusters and standard PDF card. XPS spectra of (b) Ni 2p and (c) Se 3d of NSN/CFP. (d) SEM and corresponding EDX mapping images of NSN/CFP. (e) Low-magnification TEM image of NSN/CFP with corresponding selected area diffraction pattern (top inset) and zoom-in image of one $NiSe_2$ nanoparticle (left inset). Inside the red circles are $NiSe_2$ nanoparticles, yellow line shows the boundary between the carbon fiber and the nanoparticle. (f) High-resolution TEM image of $NiSe_2$ nanoparticle and the corresponding reduced FFT image (inset) of red square area.

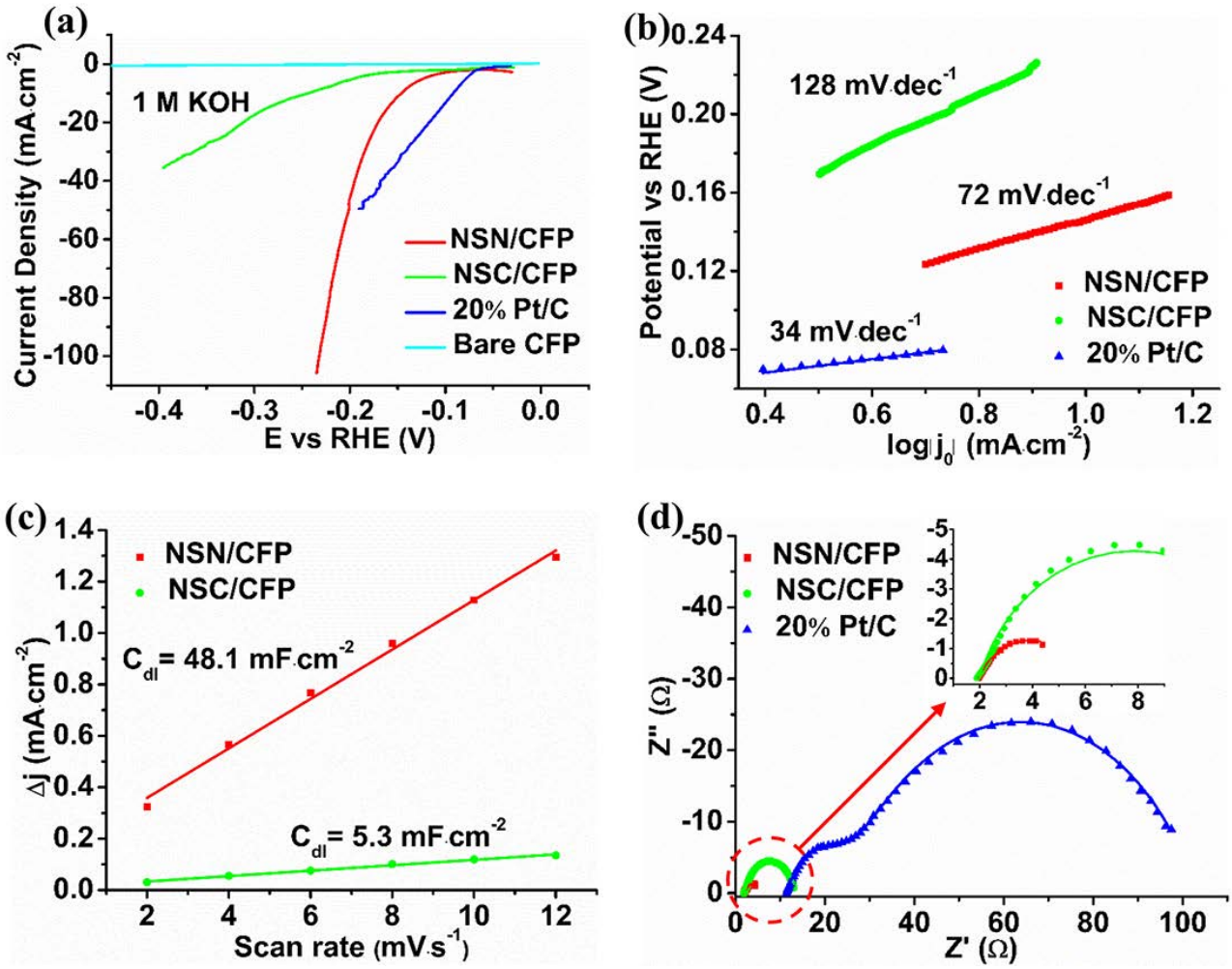

Figure 2. (a) HER linear sweep voltammetry curves of different electrocatalysts in 1 M KOH solution. (b) Tafel plots for HER in 1 M KOH. (c) C_{dl} of NSN/CFP and NSC/CFP for HER in 1 M KOH. (d) Nyquist plots of different samples reflecting the charge transfer resistance at a current density of 10 mA·cm^{-2} from 1 MHz to 10 mHz in 1 M KOH. Inset shows the zoom-in image of NSN/CFP and NSC/CFP part.

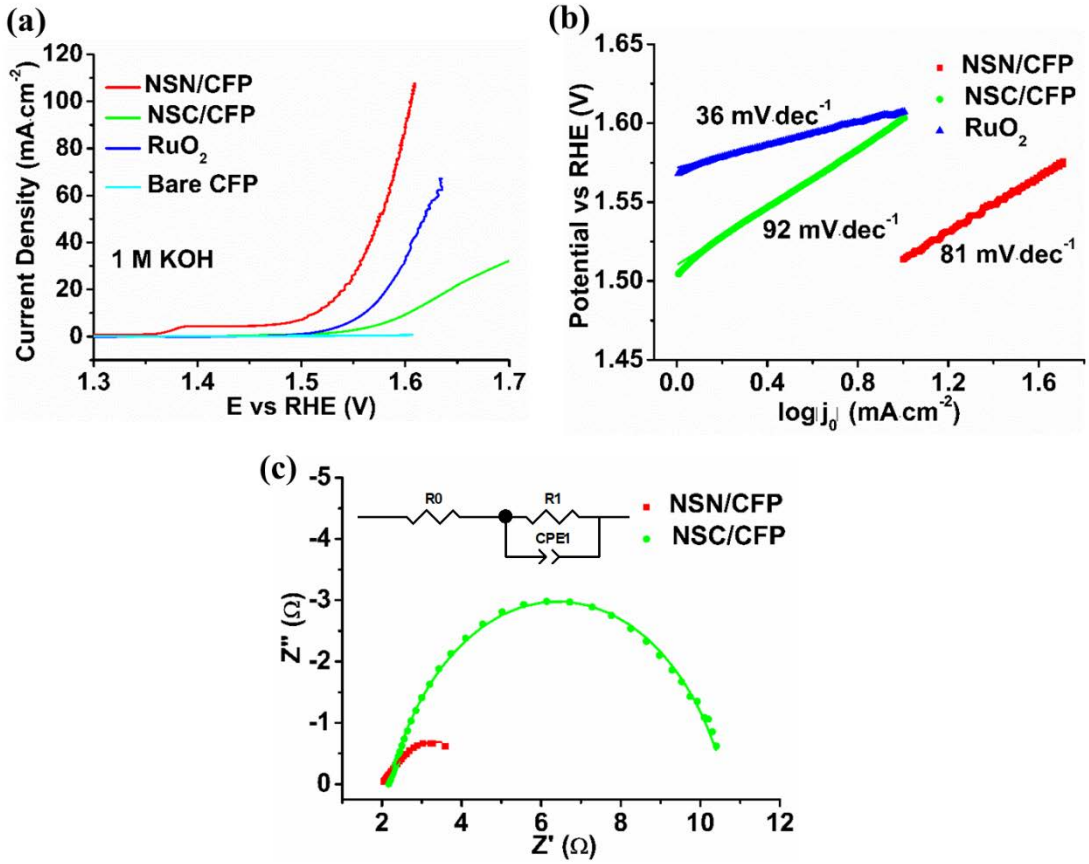

Figure 3. (a) OER linear sweep voltammetry curves of different electrocatalysts in 1 M KOH solution. (b) Tafel plots for OER in 1 M KOH. (c) Nyquist plots of different samples reflecting the charge transfer resistance at a current density of 10 mA·cm^{-2} from 1 MHz to 10 mHz in 1M KOH and the corresponding equivalent circuits.

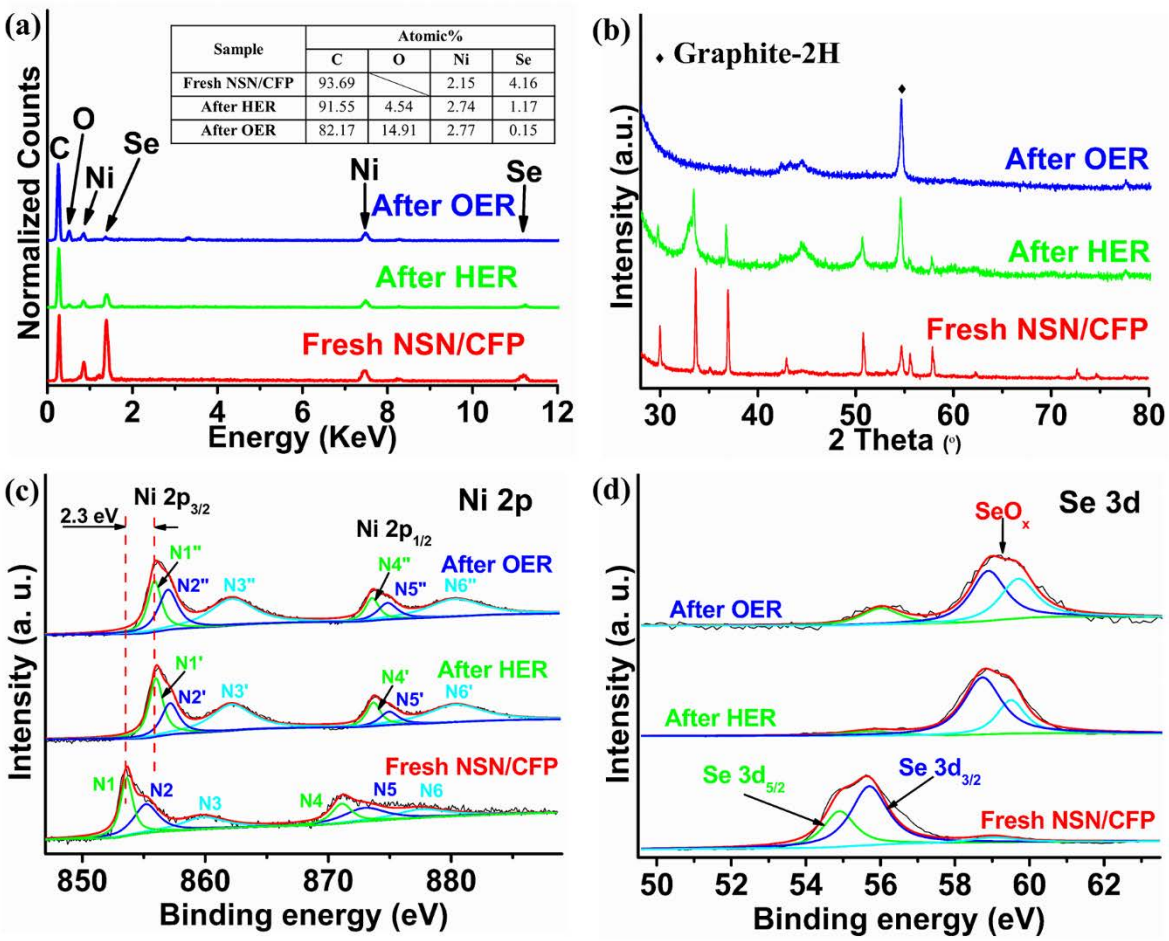

Figure 4. Comparison of (a) EDX spectra (b) XRD spectra (c) XPS spectra of Ni 2p region and (d) XPS spectra of Se 3d region of NSN/CFP before and after electrolysis.

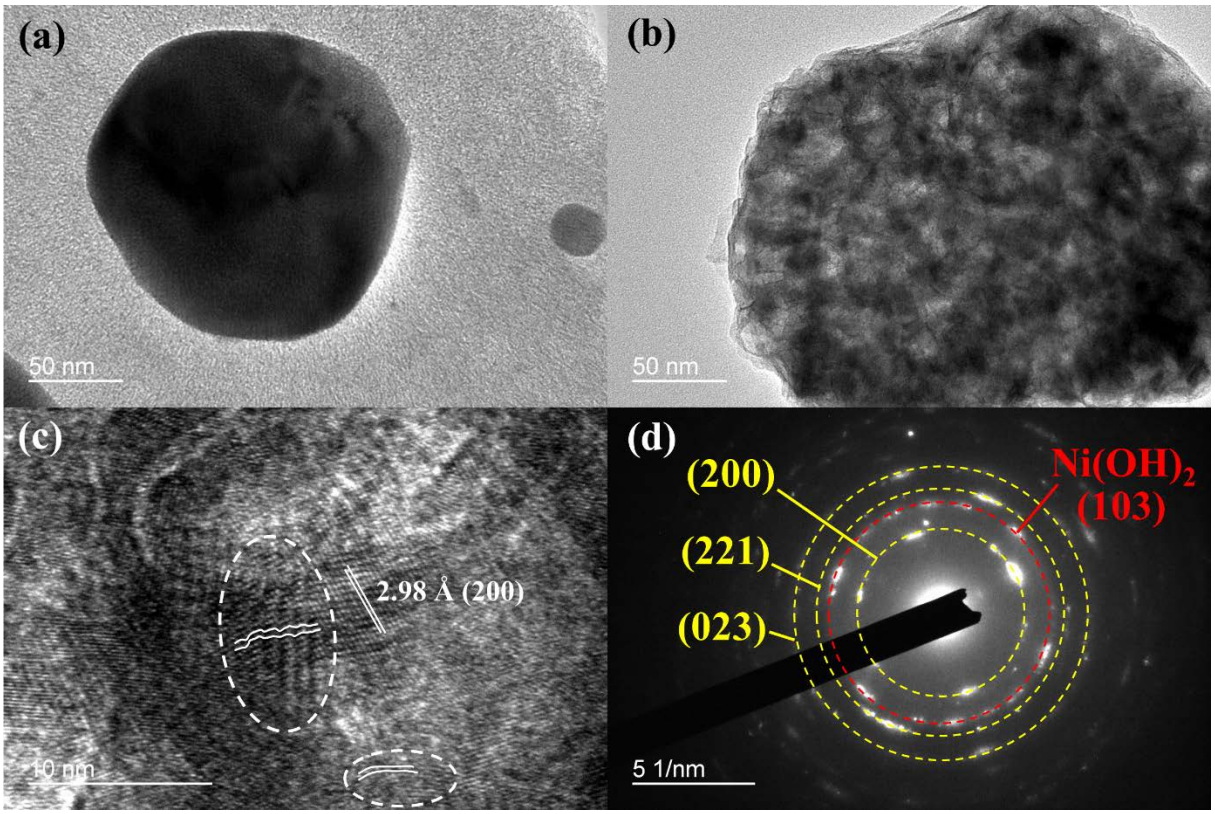

Figure 5. TEM of (a) Fresh $NiSe_2$ nanoparticles, (b) $NiSe_2$ nanoparticles after HER. (c) HRTEM image of the $NiSe_2$ nanoparticles after HER. The circles indicate the lattice distortion. (d) SAED of $NiSe_2$ nanoparticles after HER. The red circle indicates the (103) face of $Ni(OH)_2$.

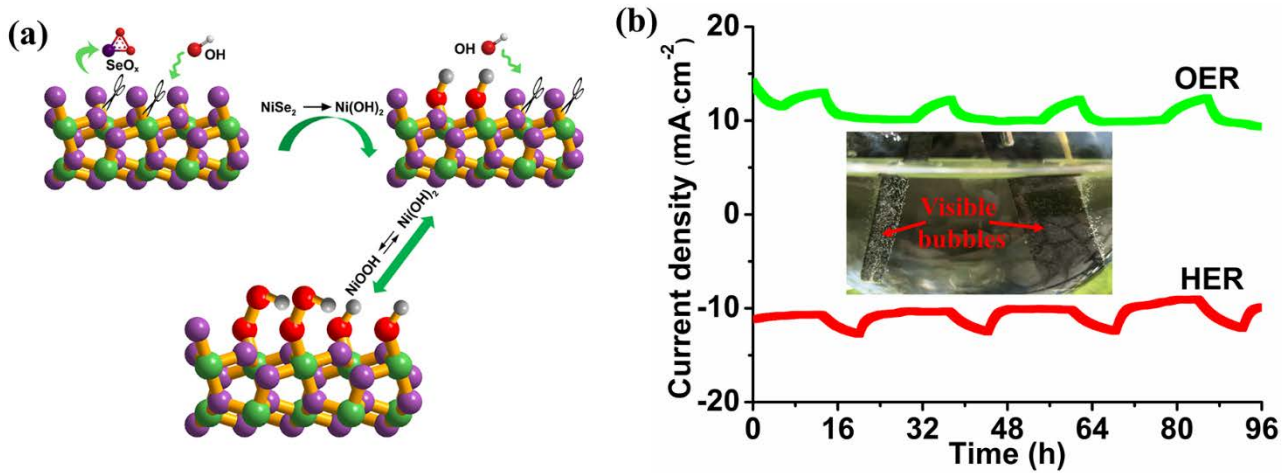

Figure 6. (a) Schematic illustration of the proposed re-construction mechanism during catalysis in alkaline medium. Atomic structure shows view towards (001) plane. Green: Ni; Purple: Se; Red: Oxygen; Gray: Hydrogen. (b) Chronoamperometric responses (j–t) test for HER and OER at constant applied potentials of −0.17 V and 1.53V versus RHE, respectively. Inset shows the photo of the generation of H_2 and O_2 bubbles during overall water electrolysis using the NSN/CFP electrodes as both cathode and anode.

Table 1. Comparison of water splitting performance of NSN/CFP in 1 M KOH with recently reported electrocatalysts at a current density of 10 $mA \cdot cm^{-2}$.

Catalyst	Reaction type	Overpotential (mV)	Tafel slope ($mV \cdot dec^{-1}$)	Refs
NSN/CFP	HER	145	72	This work
	OER	280	81	
$NiSe_2$ nanosheets	HER	42	71.1	[53]
	OER	301 @40 $mA \cdot cm^{-2}$	94.8	
$NiSe_2$ nanowires	HER	132	85.2	[54]
	OER	266	53.4	
Ni-Fe hydroxide nanosheet	HER	300	110	[55]
	OER	210	52	
Ni@N-doped graphene	HER	205	160	[56]
	OER	280	45	
NiFe hydroxide@Cu nanowire	HER	116	58.9	[57]
	OER	199	27.8	
Co_1Mn_1CH/Ni foam	HER	180	——	[58]
	OER	337 @30 $mA \cdot cm^{-2}$	——	
$Cu_{0.3}Co_{2.7}P$/N-doped carbon	HER	220	122	[59]
	OER	190	44	
N, S doped CNT	HER	400 @5 $mA \cdot cm^{-2}$	133	[60]
	OER	360	56	
Ni–Co–P hollow nanobricks	HER	107	46	[61]
	OER	270	76	